Journal of Physics D:
Applied Physics

PAPER

Growth and characterization of uranium–zirconium alloy thin films for nuclear industry applications

To cite this article: A M Adamska *et al* 2014 *J. Phys. D: Appl. Phys.* **47** 315301

IOP Publishing Journal of Physics D: Applied Physics

J. Phys. D: Appl. Phys. **47** (2014) 315301 (10pp) doi:10.1088/0022-3727/47/31/315301

Growth and characterization of uranium–zirconium alloy thin films for nuclear industry applications

A M Adamska, R Springell, A D Warren, L Picco, O Payton and T B Scott

Interface Analysis Centre, HH Wills Physics Laboratory, University of Bristol, Tyndall Avenue, Bristol, BS8 1TL, UK

E-mail: am.adamska@bristol.ac.uk

Received 18 February 2014, revised 4 June 2014
Accepted for publication 12 June 2014
Published 11 July 2014

Abstract

Polycrystalline and epitaxial U–Zr thin films have been grown on glass and single-crystal sapphire substrates using ultra-high vacuum magnetron sputtering at high temperatures ($T = 800\,^{\circ}$C). Mixed α- and γ-U phases were detected for polycrystalline U–Zr alloy thin films with the prevailing crystal structure controlled by composition. Epitaxial U–Zr thin film samples were determined to form bi-layered structures of single-crystal γ-U and α-U phases or γ-U, δUZr_2 and α-U phases depending on the concentration of the alloying element.

Keywords: U–Zr alloys, magnetron sputtering, thin films, structure, XRD, EBSD, FIB, SEM, AFM

(Some figures may appear in colour only in the online journal)

1. Introduction

As world populations continue to grow and fossil fuel supplies dwindle, there is an increasing need for alternative low-cost, carbon-neutral and secure supplies of electricity. Nuclear energy is just one solution to this problem, which has become increasingly feasible as the technology matures, yielding improvements in safety, size and efficiency. The proclaimed target for the next generation of nuclear fission reactors is to become still safer and at the same time more efficient. In the wake of the Fukishima Daiichi nuclear power plant incident there is an increased emphasis on developing improved and inherently safe materials for fuels, cladding and structural materials. The preferred choice of nuclear fuel materials is limited not only by the characteristics of the reactor cores in which they are deployed but also by their subsequent behaviour as a waste-form. The key risk posed by spent nuclear fuel involves a release of radiation that could harm human health or the environment. To date, the fuel materials that have been developed for use in power reactors include uranium and thorium metals, their alloys, oxides, carbides, nitrides and hydrides, with oxide (UO_2) as the predominant fuel type. The most desirable properties for a fuel are high melting point, thermal conductivity, compressive and tensile strength coupled with high fissionable atom density, low fabrication cost, excellent chemical and irradiation stability and exceptional corrosion resistance in conventional coolants, storage and disposal environments.

Uranium alloys materials exhibit many of these desirable properties and, based on many decades of research on bulk alloys and their use in test reactors they may now be considered as candidate future fuel materials. Pure uranium has three crystalline phases below its melting point (1405 °C) i.e. α-phase (α-U), β-phase (β-U) and γ-phase (γ-U). The room temperature (RT) α-U has a base-centred orthorhombic structure with space group *Cmcm* and unit cell parameters $a = 2.854$ Å, $b = 5.869$ Å and $c = 4.955$ Å [1, 2]. In fuels this phase shows very poor operational stability [3–5], related to highly anisotropic thermal expansion (thermal expansion coefficients for α-U single crystal over the temperature range $T = 20 - 40\,^{\circ}$C are $\alpha_{[1\,0\,0]} = -116.6 \times 10^{-6}\,^{\circ}C^{-1}$, $\alpha_{[0\,1\,0]} = -18.6 \times 10^{-6}\,^{\circ}C^{-1}$ and $\alpha_{[0\,0\,1]} = 35.6 \times 10^{-6}\,^{\circ}C^{-1}$ [6]). It also exhibits poor dimensional stability during irradiation, making it undesirable as a fuel. Irradiation growth refers to the change in uranium shape at constant volume without any external stress application. A single crystal of α-U during irradiation grows in the [0 1 0] direction, shrinks in the [1 0 0] direction and remains unchanged in the [0 0 1] direction [7]. In a polycrystalline α-U sample the extent of dimensional changes depends on the degree of preferred orientation in the

Table 1. U–Zr alloy thin film synthesis details. Note that $P_U = 100$ W, $T = 800\,^{\circ}$C, and a buffer/capping layer is Nb for all samples.

Alloying element	Substrate	Crystallinity	P (W)	Expected composition (at%)	Sputtering time (s)	Expected thickness (nm)
Zr	glass	Polycrystal	30	10	300	≈80
			60	20	300	≈86
			84	28	350	≈108
	Al_2O_3	Single crystal	32	11	300	≈75
			82	27	280	≈92

specimen. The tetragonal β-U phase exists between 668 and 775 °C, the space group is $P42/mnm$, with unit cell parameters $a = 5.656$ Å and $b = c = 10.759$ Å [8], whilst the high-temperature ($T > 775\,^{\circ}$C) γ-U has a body-centred cubic (bcc) structure with space group $Im3m$ and cell parameter $a = 3.524$ Å. This latter phase is determined to be more resistant to irradiation effects [9] than the α-phase and exhibits isotropic thermal expansion properties. Unfortunately, in pure U this phase cannot be preserved to RT, which presents a significant technical limitation. Conceptually, a solution to this problem is to stabilize the γ-phase down to RT by alloying U with another element, such as Nb, Zr or Mo, which has been achieved successfully in bulk form [9, 10]. Recently, it has also been shown that in the U–Mo system the γ-phase may be grown in thin film form as both poly- and single-crystals [11].

Epitaxially grown thin films may be used as a useful low activity experimental surrogate for bulk alloy systems, significantly reducing experimental risk and limitation [12]. They provide a simplified model surface, which can be exposed to different environmental conditions (gases, radiation and temperature) and subsequently used to predict material properties and changes in their bulk counterparts (e.g. long-term corrosion properties of U-alloy fuel materials). More fundamentally, the thin film approach to the study of actinide compounds lead to a better understanding of 5f electron systems. Thin film technology can also be used to isolate compounds or phases that may be more difficult to synthesize or even unknown in the bulk.

In this paper we explore the binary alloy phase diagram of poly- and single-crystal U–Zr thin films to see if they match. It was reported that in the bulk, the γ-U exists across almost the entire compositional range at $T > 668\,^{\circ}$C [13]. In some cases a coexistence of β-Zr phase is observed, exhibiting a bcc structure with the space group $Im3m$ and unit cell parameter $a = 3.543$ Å. For temperatures lower than 668 °C, other phases have been identified at different compositions in addition to the α-U structured alloy. Formation of δ-UZr_2 and α-Zr have been observed in bulk samples, with the former being an intermetallic primitive hexagonal phase (space group $P6/mmm$ and the unit cell parameters $a = 5.030$ Å and $c = 3.080$ Å) and the later a hexagonal close-packed (hcp) phase with the space group $P6_3/mmc$ and unit cell parameters $a = 3.232$ Å and $c = 5.147$ Å.

In this study, U–Zr poly- and single-crystal alloy thin films were grown by dc magnetron sputtering for comparison with the binary phase diagram derived for bulk alloy materials. Phase and crystallographic orientations

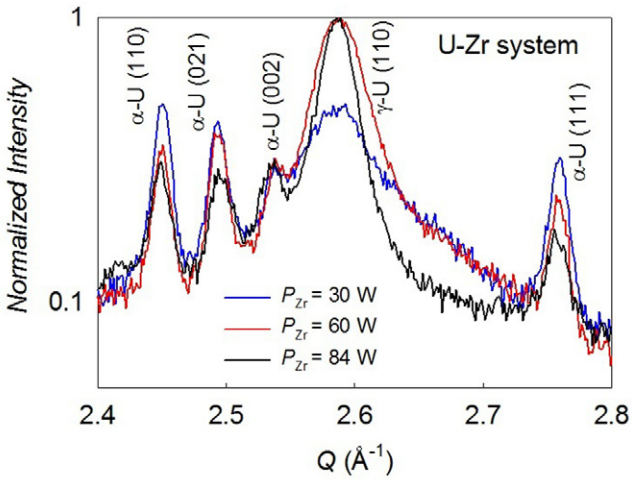

Figure 1. XRD patterns of a series U–Zr alloy thin films deposited on glass at $T = 800\,^{\circ}$C using different Zr powers.

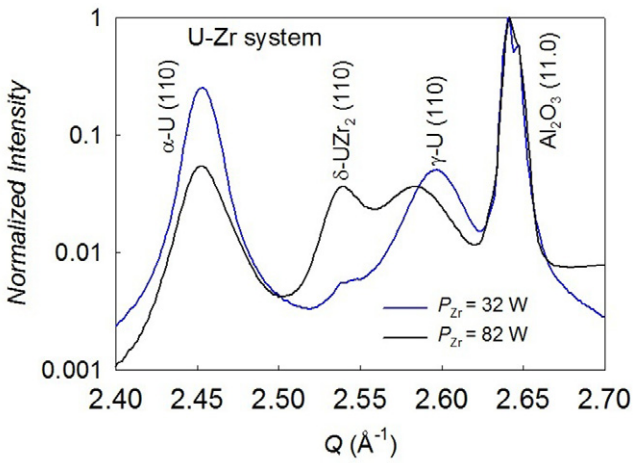

Figure 2. Comparison of the XRD patterns close to the sapphire [1 1 0] peak for single-crystal U–Zr alloy thin films deposited at $Q = 2.642\,^{\circ}$C using different Zr powers.

analysis was performed using x-ray diffraction (XRD). Film microstructure and morphology were determined using high-resolution scanning electron microscopy (SEM) and electron backscatter diffraction (EBSD). Topography and morphology of selected samples were also studied using atomic force microscopy (AFM). Energy-dispersive x-ray spectroscopy (EDX or EDS) was also used for determination and mapping of the elemental composition. The thickness of the films was initially calculated from the magnetron sputtering rates of U, Ta and Zr metals and then measured directly by cross-section

Table 2. Crystal structure details of the phases identified for U–Zr system. Note that $P_U = 100$ W, $T = 800\,^{\circ}$C, and a buffer/capping layer is Nb for all samples.

U–Zr system				
		Phase details		
P_{Zr} (W)	Crystallinity	α-U	γ-U	δUZr_2
30–84	Polycrystal	$a = 2.856\,(1)$ Å $b = 5.866\,(1)$ Å $c = 4.952\,(1)$ Å	$a = 3.428\,(1)$ Å	—
32	Single crystal	Not calculated[a]	$a = 3.417\,(1)$ Å	—
82			$a = 3.428\,(1)$ Å	$a = 4.967\,(1)$ Å c not calculated[a]

[a] Due to preferred orientation.

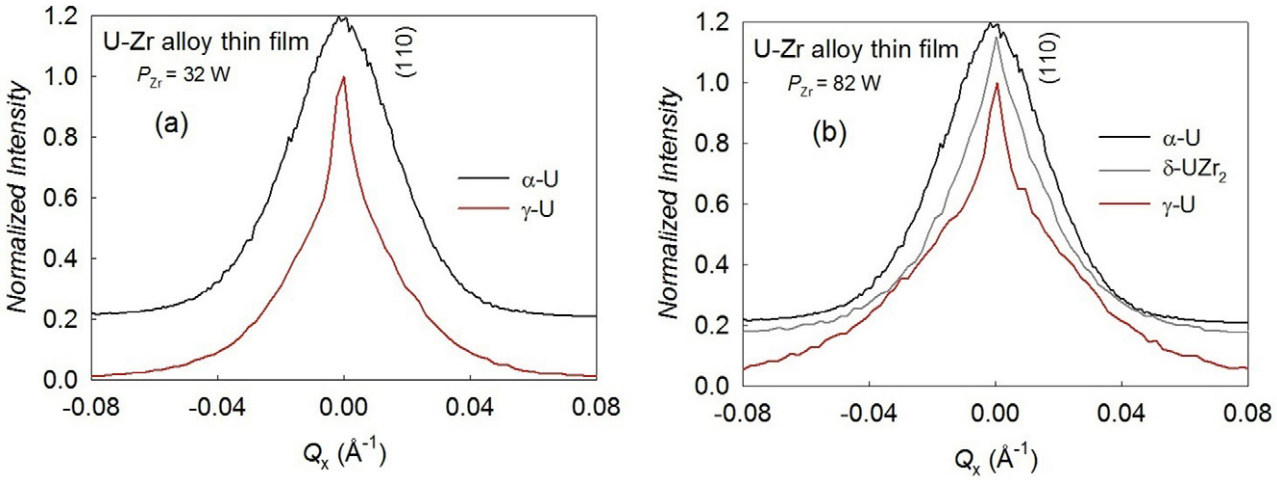

Figure 3. ω scans through the (1 1 0) reflections of (*a*) α-U and γ-U phases of double U–Zr single-crystal thin film, (*b*) α-U, δUZr_2 and γ-U phases of triple U–Zr single-crystal thin film, both deposited on sapphire substrate at $T = 800\,^{\circ}$C. The curves were shifted vertically for clarity.

analysis using combined focused ion beam (FIB) milling and SEM.

2. Experimental details

2.1. Fabrication of thin films

Poly- and single-crystal U-alloy thin films were grown using a four gun dc magnetron sputtering system with a ultra-high vacuum (UHV) base pressure of 10^{-10} mbar, *in situ* reflection high-energy electron diffraction analysis and a substrate heating stage capable of temperatures up to 800 °C. Alloy sputtering was carried out in an argon environment with a pressure of 8.0×10^{-3} mbar. The sputtering rates of U, Ta and Zr metal targets (power, $P = 100$ W) were 2.4 Å s^{-1}, 2.0 Å s^{-1} and 0.8 Å s^{-1}, respectively. Our physical vapour deposition (PVD) system allows for alloy deposition with tight control over both composition and thickness. The composition of each alloy sample corresponded to the relative power applied to each sputter gun during growth with thickness controlled by duration of sputtering. U–Zr sample synthesis details are summarized in table 1.

Substrates of size $12.0 \times 10.0 \times 1.0/0.5$ mm were plates of microscopy glass, and epitaxially polished single-crystal sapphire (Al_2O_3) of [11.0] orientation. Prior to loading into the UHV system, the substrates were cleaned by boiling successively in ultra-pure acetone, propanol and methanol. A 10 nm thick niobium buffer layer was used to seed crystalline growth of single-crystal U-alloy samples. Nb has a bcc crystal structure (space group *Im3m*) with the lattice parameter $a = 3.303$ Å and grows epitaxially at elevated temperatures with the [1 1 0] direction along the growth axis. After alloy deposition a protective capping layer of Nb (5–10 nm) was deposited to prevent atmospheric attack. A prior study of epitaxial [1 1 0] Nb films deposited on sapphire shows that a stable (2.0 nm thick) layer of Nb_2O_5 is formed, which provides effective long-term passivation [14].

2.2. Phase distribution, microstructure and topography

For phase analysis, XRD experiments were performed using a Philips X'PERT X-ray diffractometer with Cu-Kα radiation ($\lambda = 1.54$ Å). Conventional θ–2θ and ω scans were recorded for each sample.

SEM and FIB milling were used to examine the microstructure of the samples produced. The FIB in this study was a FEI FIB Strata 201 FIB system (operating under a background pressure of better than 10^{-5} mbar) with a gallium

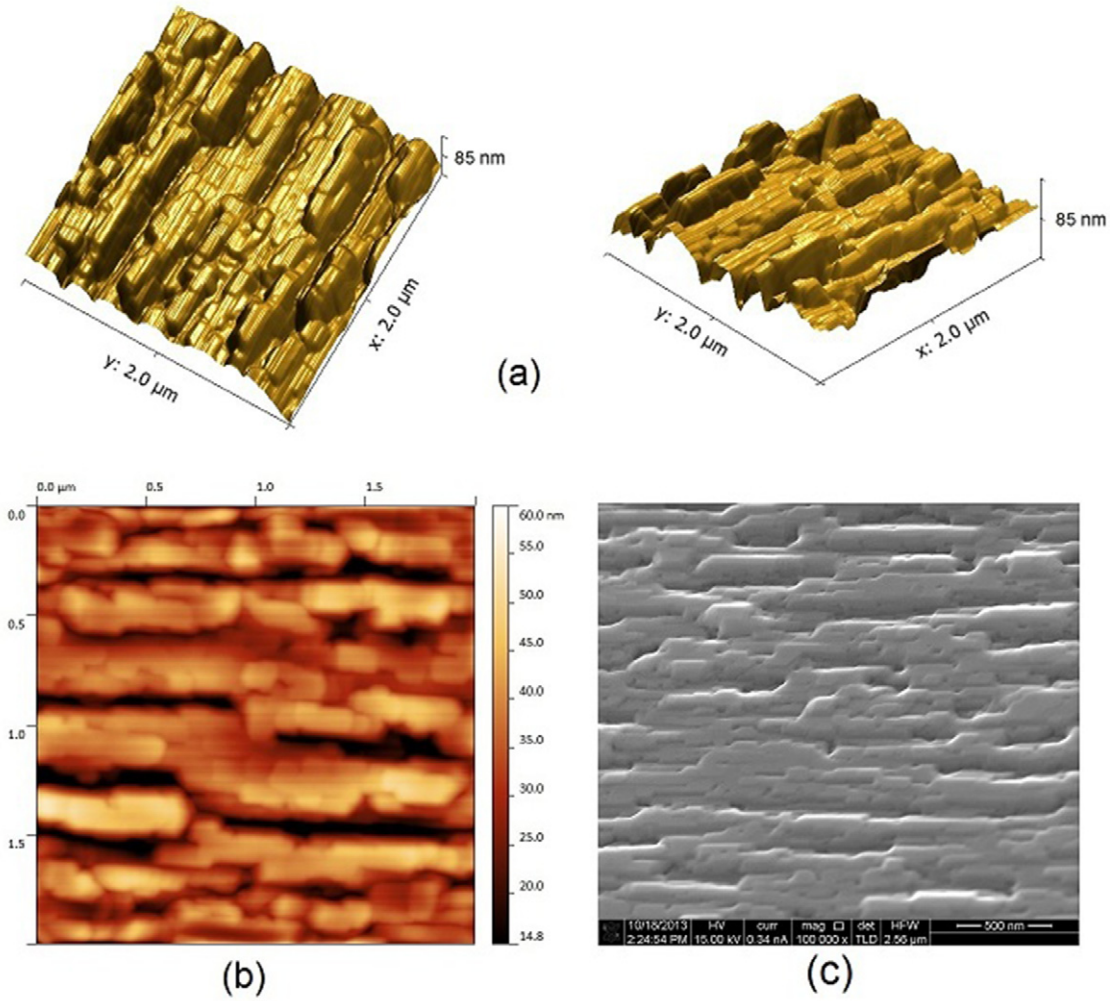

Figure 4. AFM (*a*) topography of the double U–Zr single-crystal thin film sample seen under different angles, (*b*) micrograph and (*c*) SE image of the surface of the double U–Zr single-crystal thin film sample.

ion source. The SEM was a ZEISS Σigma™ field emission scanning electron microscopy (FEG-SEM) fitted with in-lens Everhart-Thornley type secondary electron detectors with additional EBSD and EDS instrumentation from AMETEK-EDAX. The diffraction data acquired from EBSD analysis was recorded and processed using OIM™ software, which produced crystallographic orientation and phase maps from predefined surface areas using an automated mapping routine.

AFM data were collected using a Dimension 3100 AFM (Bruker, Germany) operated in contact-mode and using cantilevers with a nominal spring constant of 0.01 N m^{-1} and tip radius of 2 nm (MSNL, Bruker). Measurement sites were randomly selected across the whole 10 × 10 mm^2 sample surface. Images were collected at 2, 5, 20 and 20 μm scan size with 512 × 512 pixel per image at a line rate of 2 Hz. Repeated scans of the same regions revealed no signs of cantilever-tip-derived sample degradation.

2.3. Composition and thickness measurements

The thickness of the U–Zr thin films was measured in a Helios X600 DualBeam (DB) instrument (a combined FIB-SEM instrument). A protective platinum coating was deposited on selected areas of the surface followed by ion beam sectioning to a depth of 2–3 μm. The thickness of the thin film layer was measured using high-magnification SEM.

EDS (or EDX) spectra/maps were collected from the surface of the U–Zr thin films using both DB and FEG-SEM instruments, both running a Peltier cooled silicon drift detector EDX instrument.

3. Results and discussion

3.1. Polycrystalline U–Zr thin films

Polycrystalline U–Zr alloy thin films were grown on glass substrates at $T = 800\,^{\circ}$C. A sputtered layer of Nb metal was used as a buffer/capping layer (10 nm thick). Comparative XRD patterns recorded from U–Zr alloy thin films grown at different Zr powers ($P_{Zr} = 30, 60, 84$ W) are shown in figure 1. All samples reveal the coexistence of both α-U and γ-U phases.

The γ-U reflection (1 1 0) is positioned at 2.589 Å for all samples. Its intensity for the samples synthesized using $P_{Zr} = 60$–84 W is higher than that for the α-U phase,

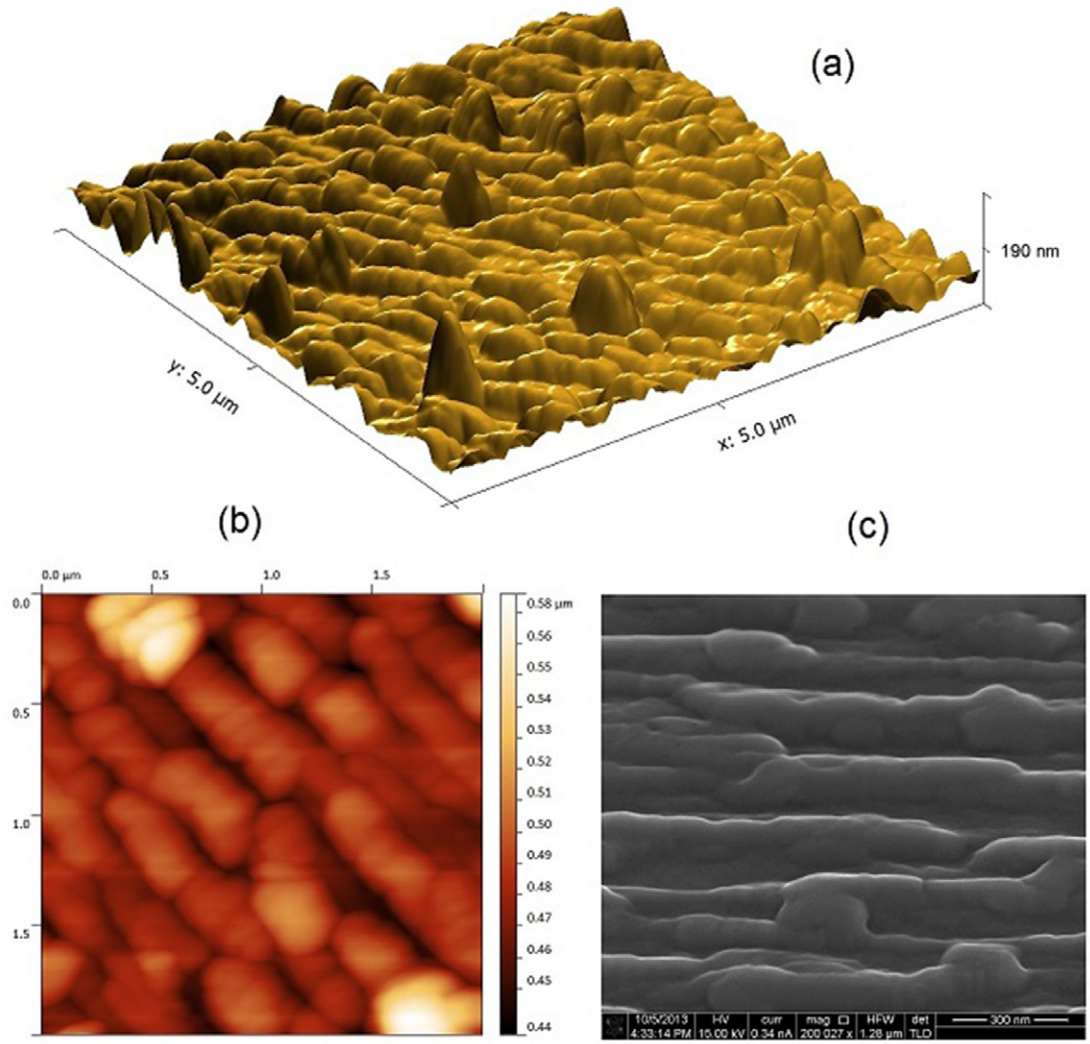

Figure 5. (*a*) AFM topography, (*b*) AFM micrograph and (*c*) SE image of surface of the triple U–Zr single-crystal thin film sample.

which suggests the predominance of the γ-U phase in those samples. In the case of the sample synthesized at $P_{Zr} = 30$ W, the γ-U reflection (1 1 0) intensity is lower than that of the α-U reflections, which is ascribed to a proportionally greater volume of α-U phase. The α-U (1 1 0), (0 0 2) and (1 1 1) peaks are positioned at 2.449(1) Å^{-1}, 2.537(1) Å^{-1} and 2.759(1) Å^{-1}, respectively, which is in agreement with the bulk α-U data from Wyckoff (1965), where $Q = 2.448$ Å^{-1} for α-U (1 1 0), $Q = 2.536$ Å^{-1} for α-U (0 0 2) and $Q = 2.757$ Å^{-1} for α-U (1 1 1) [15]. Only trace amounts of UO_2 were also detected by XRD, this was considered to be insufficient to affect the stability of alloy phases. The failure in synthesis of a single γ-U phase at $T = 800\,^{\circ}$C can ascribed to an insufficiently high substrate temperature (thermocouple is attached to the heater, not to the sample holder) or too slow a rate of cooling.

The composition of the alloys was again determined using EDX analysis (the spectra were collected from the surface of the samples), yielding values of 9.2 at%, 18.6 at% and 25.5 at% Zr for the samples synthesized at $P_{Zr} = 30$ W, 60 W and 84 W, respectively. These values are close to those calculated from sputtering powers, see table 1. The measured thickness of the thin film layers was 80–120 nm, which is also in good agreement with the calculated values of thickness, see table 1. What is of significance is that all samples consist of two crystallographic phases and only one, i.e. γ-U accommodates Zr atoms in any significant abundance.

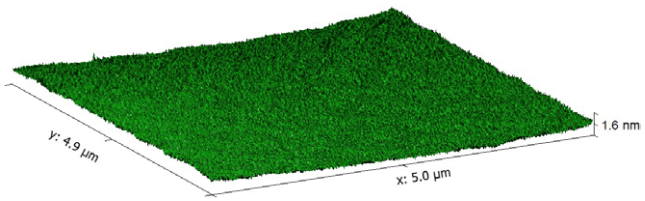

Figure 6. AFM topography of the single-crystal sapphire substrate.

3.2. Single-crystal U–Zr thin films

Single-crystal U–Zr alloy thin films were grown and seeded with Nb buffer layers (10 nm thick) on single-crystal sapphire substrates at $T = 800\,^{\circ}$C. All samples were subsequently capped with a protective Nb layer (5 nm thick) after cooling

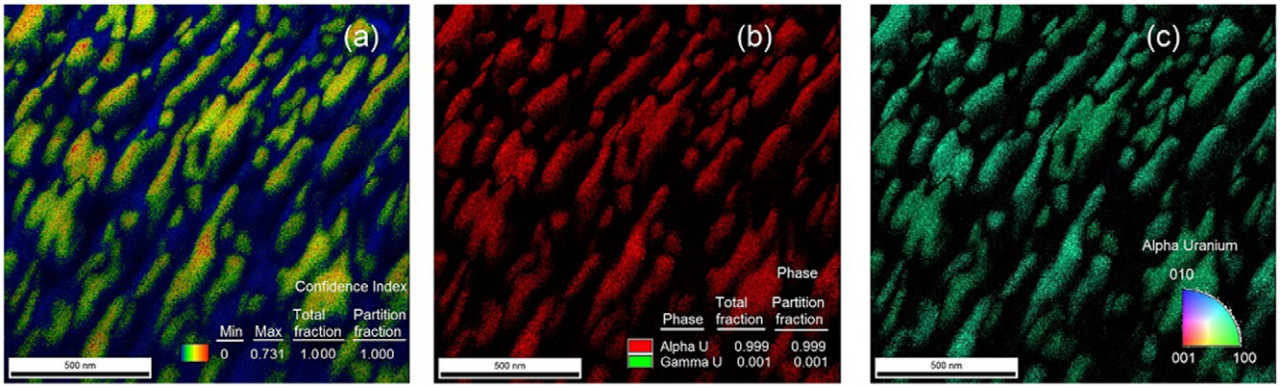

Figure 7. EBSD maps of the double U–Zr single crystal showing (*a*) confidence index for the recognized phase, (*b*) phase fractions and (*c*) the inverse pole figure showing the orientation of the single crystal.

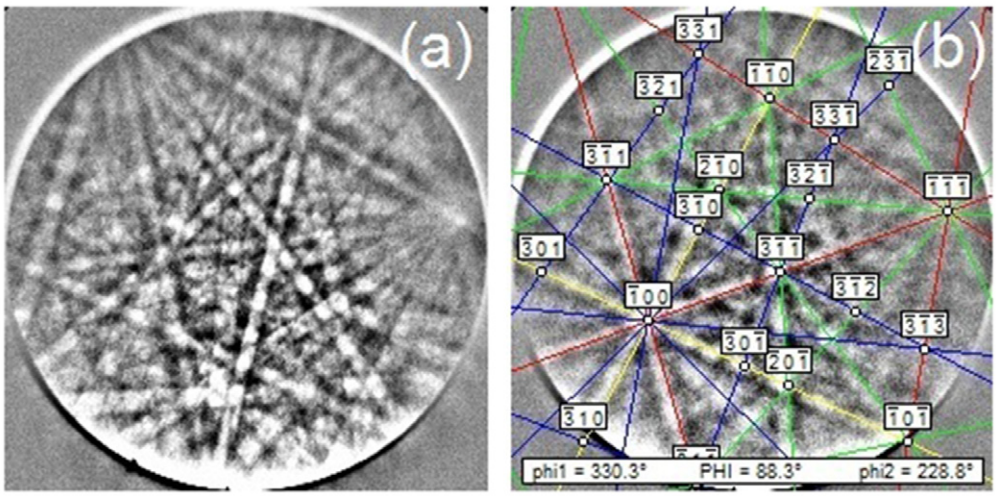

Figure 8. EBSD patterns collected (*a*) at the surface of the double U–Zr single crystal, showing overlapped bands of α- and γ-U phases (*b*) after removal of the signal from the α-U phase, showing the indexed bands of γ-U phase.

to RT. The XRD patterns of the single-crystal U–Zr alloy thin films grown at $T = 800\,^{\circ}\mathrm{C}$ are shown in figure 2. The signal intensity is normalized to unity on the peak of the scattering recorded from the epitaxial sapphire substrate at $Q = 2.642\,\text{Å}^{-1}$.

In the case of the sample synthesized using $P_{\mathrm{Zr}} = 32\,\mathrm{W}$, two main phases α- and γ-U are identified (double U–Zr single-crystal sample). For the sample synthesized using $P_{\mathrm{Zr}} = 82\,\mathrm{W}$, three distinct phases (α-U, γ-U and δUZr_2) are observed (triple U–Zr single-crystal sample). All identified phases exhibit a [1 1 0] orientation on sapphire when deposited at $T = 800\,^{\circ}\mathrm{C}$. The γ-U (1 1 0) is observed at $2.596(1)\,\text{Å}^{-1}$ and$2.585(1)\,\text{Å}^{-1}$ for the samples synthesized at $P_{\mathrm{Zr}} = 32\,\mathrm{W}$ and 82 W, respectively. The α-U (1 1 0) is located at $2.452(1)\,\text{Å}^{-1}$ for both samples. The δUZr_2 (1 1 0) is seen at $2.539\,\text{Å}^{-1}$. Similarly in this case, the failure in synthesis of a single γ-U phase at $T = 800\,^{\circ}\mathrm{C}$, chosen according to the phase diagram [13], can be ascribed to an insufficiently high substrate temperature or too slow a rate of cooling. Although, the existing phase diagram has been constructed base on the data available for bulk U–Zr counterparts, and it can be different for low-dimensional thin film samples. In addition, it has been shown that in the case of U-30 at% Zr alloy the $\gamma \rightarrow \delta$ phase transition takes place by so-called omega transformation mechanism; in which the alternate (1 1 1) planes of parent γ-phase collapse to form AlB_2 type hexagonal structure [16]. The $\gamma \rightarrow \delta$ omega transformation can take place either athermally or isothermally. Quenching from high γ-field results in athermal δ formation with less amount of retained γ-phase. Quenching temperature just above the $\gamma \rightarrow \delta$ transition causes full retention of metastable γ-phase. No traces of UO_2, UC or other impurity phases have been detected by XRD, suggesting efficient fabrication and subsequent integrity of the capping Nb layer. To help with further discussion the crystallographic information for poly- and single-crystal U–Zr thin films are summarized in table 2.

As shown in table 2, the calculated lattice parameter of the observed γ-U bcc structures is lower than previously reported for bulk γ-U samples. Additionally, δUZr_2 is only observed for single-crystal samples and not the polycrystalline films of equivalent composition.

In order to check the crystallographic quality of the samples, ω scans was performed by rocking the sample through the Bragg position, whilst keeping the detector in a fixed position so that the scattering vector runs parallel to Q_x, where Q_x is the x component of the scattering vector Q, which is

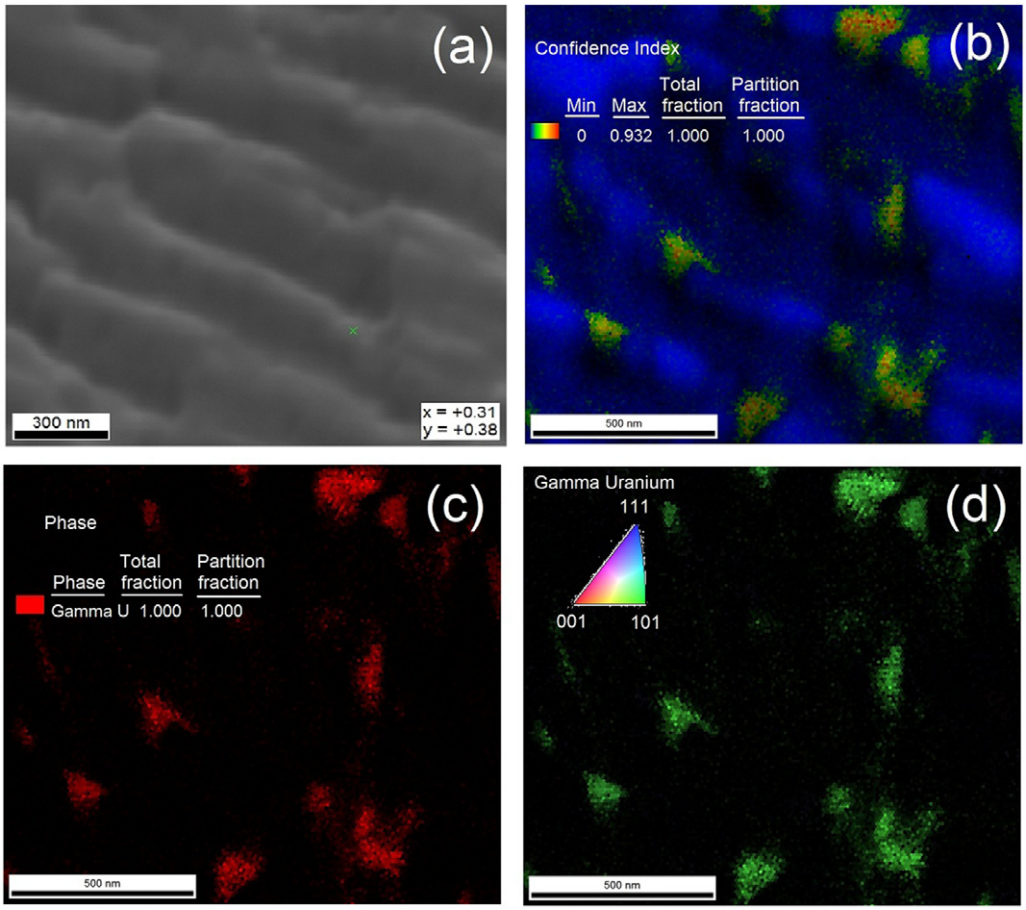

Figure 9. (*a*) SE image of the surface of U–Zr sample, (*b*) EBSD map showing confidence index for the recognized phase, (*c*) phase fraction and (*d*) the inverse pole figure showing the orientation of the single crystal.

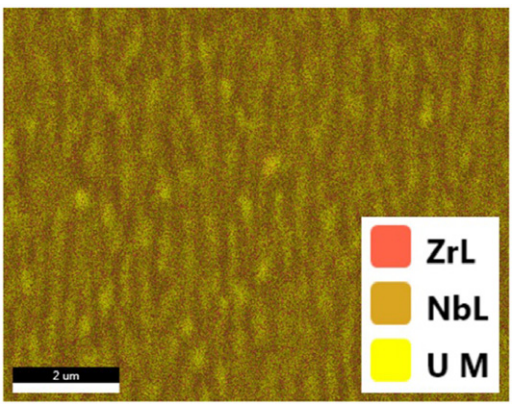

Figure 10. EDS maps collected at the surface of the double U–Zr single crystal.

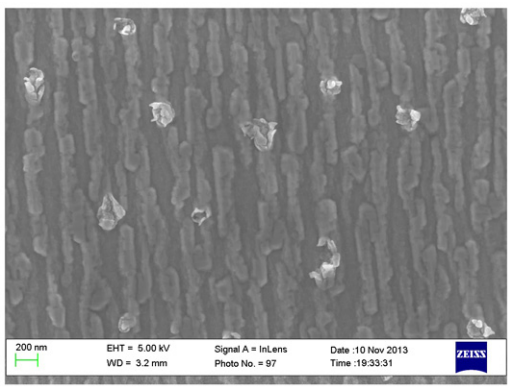

Figure 11. SE image of the surface of oxidized triple U–Zr single-crystal thin film sample.

parallel to the sample surface. This component can be obtained from the ω and θ angles using $Q_x = (4\pi/\lambda)\sin\theta\,\sin(\omega - \theta)$ (Å^{-1}) [17, 18]. Thus, the rocking curves through the (1 1 0) reflections of α-U, γ-U and δUZr_2 phases of U–Zr single-crystal alloy thin films were measured, see figure 3. Two components are observed in the rocking curves through the (1 1 0) reflection of the γ-U phase, a narrow peak with full-width at half-maximum (FWHM) $\approx$ 0.14° and a broader peak with FWHM $\approx$ 1.0° for the samples synthesized using $P_{Zr} = 32$ W, and FWHM $\approx$ 0.16° (a narrow peak) and $\approx$1.6° (a broad peak) for the sample synthesized using $P_{Zr} = 82$ W. Both components were also identified for the δUZr_2 (1 1 0) reflection with FWHM $\approx$ 0.2° for a narrow peak and $\approx$1.1° for a broad peak. In the case of the α-U (1 1 0) reflection, only one broad rocking curve component (FWHM $\approx$ 1.0°) was observed. The rocking curve width indicates coherency across the film–substrate interface and also the capping layer. The appearance of two components in the rocking curves may be explained by the existence of two distinct phases in the film, one of almost perfect crystalline form associated with large

flat regions (the narrow Gaussian-shape component) and other a relaxed, dislocated layer (the broad Lorenzian squared-shape component). According to the 'perfect-layer model' [19] the 'perfect phase' is often assumed to be that positioned closest to the substrate, growing strained and pseudomorfically, i.e. with the same in-plane lattice parameter as the substrate. As the material is grown above a critical thickness, the formation of defects is increasingly energetically favourable and the relaxed or defective phase begins predominate growth and comprises the rest of the sample deposited on top. The appearance of the narrow component may be also an indication of extreme flatness (on average) of the atomic planes parallel to the surface of the film [20] or long-range orientational order [21].

Based on the 'perfect-layer model' one can assume that in the current case, the sample synthesized using $P_{Zr} = 32$ W had γ-U phase growing directly on the Nb buffer layer and subsequently a dislocated α-U phase was spontaneously grown on the top. For the triple single-crystal sample, one can speculate that two phases, γ-U and δ-UZr_2, grow directly on the Nb buffer layer (both rocking curves through (1 1 0) reflections of these phases have narrow components) overlain by the α-U. Previous studies of single-crystal α-U grown on a Nb buffer layer of thickness between 3 and 30 nm showed that all rocking curves through the α-U (1 1 0) reflection exhibit a narrow component [22]. For U-films grown on a much thicker Nb buffer layers (60–130 nm), the narrow component vanishes, which suggests that any accumulating disorder in the Nb layer is magnified in the overlying U layer. In these previous studies the thickness of U layers was only 11–19 nm. In order to confirm the arrangement of the determined U phases in our current single-crystal samples, EBSD data were collected. The surface topography of the double U–Zr single-crystal sample is shown in figures 4(*a*) and (*b*), exhibiting a surface morphology of sharply stepped ridges. SE image of surface of the sample (figure 5(*c*)) reveals small ($\approx 5.0 \times 5.0$ nm^2) square or rectangular holes ascribed as gaps or windows in the upper 'dislocated' layer revealing the underlying 'perfect' film.

Table 3. Summary of results for U–Zr system.

	U–Zr system	
	Polycrystalline	Single Crystal
Alloy phase	γ-U	γ-U
Intermetallic phases	α-U	α-U and δUZr_2
Impurity phase	UO_2	—
Rocking curves	—	α-U—one component (FWHM $\approx 1.0^\circ$) γ-U and δUZr_2— two components (e.g. FWHM $\approx 0.14^\circ$ and 1.0°)
Orientation	Random	(1 1 0)
Morphology	Flat surface	Rectangular/circular ridges

The topography of the triple U–Zr single crystal exhibits a ridged surface morphology that was comparatively more rounded, see figure 5(*a*). These surface ridges are likely to be connected with a strain relief phenomenon [23]. White dots on the surface of the sample seen on AFM micrographs (figure 5(*b*)) show oxide development assumed to arise in areas where the local morphology induced a shadow zone during Nb sputtering that left the bare alloy surface exposed to oxidation when removed to air. No obvious windows in the surface were observed by SEM (figure 5(*c*)).

As revealed by combined AFM and SEM, the surface of the samples is not perfectly flat as would usually be expected for thin film samples. Accordingly, the narrow component of the rocking curves observed for the γ-U reflections during XRD analysis does not originate from the flatness of the sample. AFM topography recorded for a single-crystal sapphire substrate (figure 6) shows an extremely flat surface, which means the observed ridged surface for our U–Zr thin films does not originate from the substrate morphology.

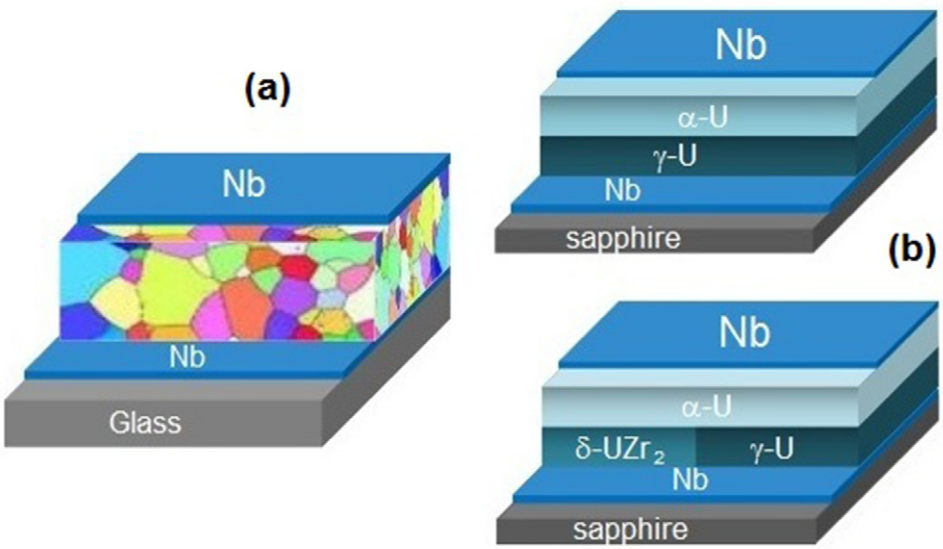

Figure 12. Schematic representation of thin film layer structure for (*a*) polycrystal and (*b*) single crystal of U–Zr alloys.

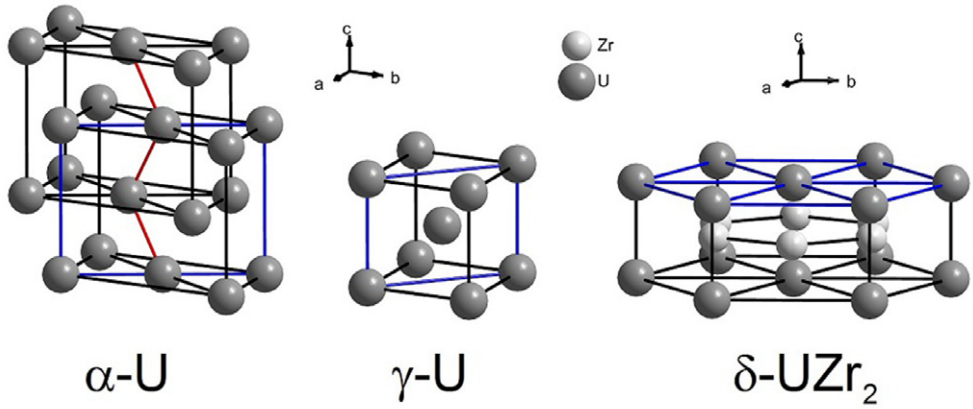

Figure 13. Unit cells of α-U, γ-U and δUZr_2, the (1 1 0) planes are indicated in blue. The chain structure of α-U with the shortest U–U distances of 2.754 Å is indicated red.

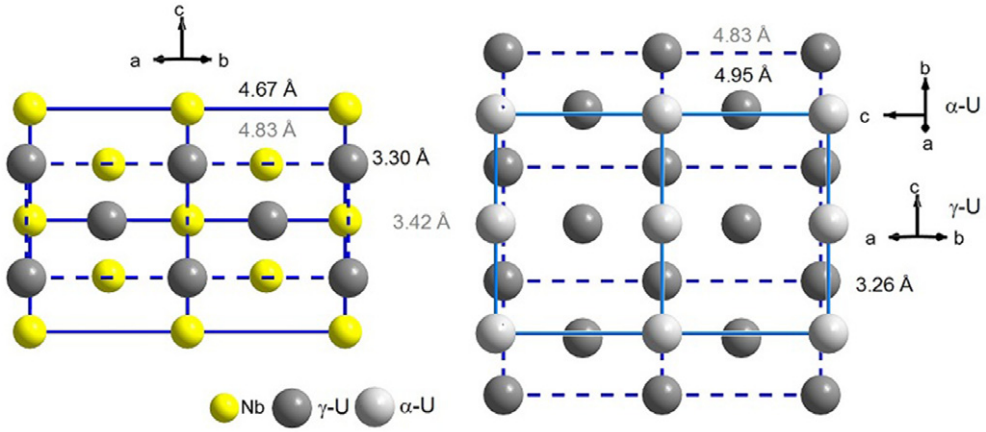

Figure 14. Two-dimensional projection illustrating possible growth of the γ-U on Nb buffer layer (left) and α-U on γ-U layer (right).

In addition, such a ridged surface inflicts limitations for EBSD mapping. EBSD is an extremely surface sensitive diffraction mapping technique with a sampling depth of between 5.0 and 10.0 nm depending on the material being analysed. Consequently it is very well suited to the investigation of surfaces, which are pristinely flat, e.g. thin films which may have initially grown epitaxially on a selected substrate but later exhibited more randomized crystal growth. EBSD maps recorded from the surface of the double U–Zr single crystal sample (see figure 7) indicated an α-U single-crystal located on top of the film. This phase was recognized with a highest confidence index (up to 0.731) on top of the observed ridge structures with the lowest confidence for indexing recorded in the troughs ascribed to morphology effect.

γ-U phase was not detected on the surface of the sample. However, EBSD patterns taken at the surface of the samples in the troughed zones showed overlapped patterns of α-U and γ-U phases (figure 8(a)). In order to detect a signal from the buried γ-U phase layer, the α-U phase was filtered out from the indexing process using the OIM software (figure 8(b)). The γ-U phase was then detected and indexed with high confidence index (up to 0.932). Figure 9 shows EBSD maps collected for double single-crystal U–Zr thin film, showing the distribution of the γ-U phase, coinciding with 'window' regions in the overlying α-U layer.

EBSD maps collected for the triple U–Zr single crystal (not shown here) also exhibited a α-U single crystal located on the top of the film, although the quality of the mapping was much worse than for the double single-crystal sample, thus the detection of γ-U and δUZr_2 phases was much more difficult. Ion sputtering (Ga^+ ions) attempts to remove the top layer of the sample were found to induce too much implantation damage to make successful EBSD mapping possible.

The double U–Zr single-crystal layer thickness was measured to be between 20 nm (bottom later) and 80 nm (height of the ridges), while the thickness of the triple U–Zr single crystal was between 50 nm (bottom layer) and 150 nm (height of the ridges). These values are different than the thicknesses calculated (table 1) for assumed homogeneously flat samples.

In order to verify the composition of the alloys, EDS spectra and maps were acquired from the surfaces of the samples. An example of an EDS map collected for the double U–Zr single-crystal thin film sample is shown in figure 10. The final compositions of the U–Zr alloys are $U_{0.8}Zr_{0.2}$ for the double single-crystal and $U_{0.6}Zr_{0.4}$ for triple single-crystal, these values are different from the values calculated in table 1 and values for polycrystalline samples. According to the

crystal structure data the lattice parameter of the single crystal synthesized using $P_{Zr} = 32$ W is smaller than the lattice parameter of the polycrystalline thin film sample, which is ascribed to the accommodation of more Zr atoms in the γ-U phase. The ratio of γ-U alloy phase to the pure α-U phase is higher for the single-crystal sample than for polycrystalline samples. In the case of triple single-crystal phase, Zr atoms are not only accommodated by the γ-U phase but also by the δUZr_2 phase.

After exposition of U–Zr thin samples to air for a month, the peculiar oxide development ascribed to morphology of the samples was observed (see figure 11). Some discrete regions of the ridges not protected sufficiently by the protective Nb layer, showing 'flower-like' growth of UO_2.

4. Summary and conclusions

The key in developing an effective alloy fuel is in stabilizing a wholly γ-phase material. Previous work has shown that it is possible to grow an almost perfect single γ-phase U–Mo thin film on a sapphire substrate using a Nb buffer layer [11]. For the U–Zr system studied here the coexistence of α-U, γ-U and δUZr_2 phases was reported. A single γ-U phase thin film could not be grown, which is ascribed at present to an insufficiently high substrate temperature or too slow a rate of cooling or the $\gamma \rightarrow \delta$ transition took place. The results obtained for U–Zr poly- and single-crystal thin films are summarized in table 3. Figure 12 shows a schematic representation of the thin film layer structure observed in the U–Zr system. Figure 13 shows units cells of α-U, γ-U and δUZr_2, the (1 1 0) growth planes are indicated in blue.

Based on the XRD data of α-U grown on a Nb buffer layer along the [1 1 0] direction presented by Ward *et al* and Springell *et al* [24, 25], one can derive the epitaxial relationship between the Nb buffer layer and γ-U or δUZr_2 and α-U. As was shown by the EBSD mapping and the narrow rocking curve component, γ-U grows on the (1 1 0) plane of Nb. In figure 14, one of the possible γ-U and α-U domains are shown.

In order to determine the real epitaxial relationship between Nb buffer layer, γ-U, δUZr_2 and α-U, the measurement of inclined (off-axis) Bragg reflections will be performed. For chosen off-axis reflections the sample will be rotated about the growth axis (ϕ scan) until a reflection is found. A full rotation about ϕ will show the angles at which the reflections occur and angles between the peaks will provide information to identify the in-plane orientation relationship between the respective single-crystal layers.

In addition, U–Mo and U–Zr alloys were found to be superconducting below 2 K or 1.3–0.6 K, respectively [26, 27]. Thus, the studies of magnetic and superconducting properties of single-crystal γ-U phase alloys would provide a unique set of data as these properties have never been investigated for U-alloys in single-crystal form.

Acknowledgments

People Marie Curie Actions (EU FP7), Intra-European Fellowships (IEF), Project: URALLOY(2012–2014) and Royal Academy of Engineering.

References

[1] Barrett C S, Mueller M H and Hitterman L R 1963 *Phys. Rev.* **129** 625
[2] Lander G H and Mueller M H 1970 *Acta Cryst.* B **26** 129
[3] Holden A N 1958 *Physical Metallurgy of Uranium* (Reading, MA: Addison-Wesley)
[4] Ostberg G, Moller M and Chonning-Christiansson B S 1963 *J. Nucl. Mater.* **10** 329
[5] Keiser D D Jr, Robinson A B, Jue J-F, Medvedev P, Wachs D M and Finlay M R 2009 *J. Nucl. Mater.* **393** 311
[6] Lloyd L T and Barrett S C 1966 *J. Nucl. Mater.* **18** 55
[7] Lloyd L T 1961 *J. Nucl. Mater.* **3** 67
[8] Roy P R and Sah D N 1985 *J. Phys.* **24** 397
[9] Donohue J and Einspahr H 1740 *Acta Cryst.* B **27** 1740
[10] Bleiberg M L, Eichenberg J D, Fillnow R H and Jones L J (ed) 1957 *Development and Properties of Uranium-base Alloys Corrosion Resistant in High Temperature Water: Radiation Stability of Uranium-Base Alloys, Part 4* (Bettis Plant) p 7–38
[11] Sinha V P, Hegde P V, Prasad G J, Dey G K and Kamath H S 2010 *J. Alloys Compounds* **506** 253
[12] Adamska A M, Springell R and Scott T 2014 *Thin Solid Films* **550** 319–25
[13] Seibert A, Stumpf S, Gouder T, Schild D and Denecke M A 2011 *Actidine Nanoparticle Research: Actinide Thin films as Surface Models* (Berlin: Springer) pp 275–313
[14] Okamato H 2007 *J. Phases Equilib. Diffusion* **28** 499–500
[15] Hellwig O, Song G, Becker H W, Birkner A and Zabel H 2000 *Mater.wiss. Werkst.tech.* **31** 856
[16] Wyckoff R 1965 *Crystal Structures* 2nd edn vol 1 (New York: Interscience)
[17] Basak C B, Prabhu N and Krishnan M 2010 *Intermetallics* **18** 1707–12
[18] Boulle A, Guinebretière R, Masson O, Bachelet R, Conchon F and Dauger A 2006 *Appl. Surf. Sci.* **253** 95
[19] Boulle A, Masson O, Guinebretière R, Lecomte A and Dauger A 2002 *J. Appl. Cryst.* **35** 606
[20] Stierle A, Abromeit A, Metoki N and Zabel H 1993 *J. Appl. Phys.* **73** 4808–14
[21] McMorrow D F, Cowley R A, Gibaud A, Ward R C C and Wells M R 1993 *Appl. Phys. Lett.* **63** 2195–7
[22] Wölfing B, Theis-Bröhl K, Sutter C and Zabel H 1999 *J. Phys.: Condens. Matter* **11** 2669
[23] Chivall J 2012 Growth and characterisation of uranium nanostructures *PhD Thesis* p 124
[24] Jiang H, Khang D-Y, Song J, Sun Y, Huang Y and Rogers J A 2007 *Proc. Natl Acad. Sci.* **104** 15607
[25] Ward R C C, Cowley R A, Ling N, Goetze W, Lander G H and Stirling W G 2008 *J. Phys.: Condens. Matter* **20** 135003
[26] Springell R, Detlefs B, Lander G H, Ward R C C, Cowley R A, Ling N, Goetze W, Ahuja R, Luo W and Johansson B 2008 *Phys. Rev.* **78** 193403
[27] Berlincourt T G 1959 *J. Phys. Chem. Solids* **11** 12